TOPICAL COLLECTION: INNOVATIONS IN HIGH ENTROPY ALLOYS AND BULK METALLIC GLASSES

Triaxial Constraint and Tensile Strength Enhancement in Brazed Joints

XIN CAI, YANFEI GAO, XUE WANG, WEI ZHANG, WEI LIU, XINPU SHEN, WEI ZHANG, ZHENZHEN YU, and ZHILI FENG

A brazed joint consists of a low-melting point and thin interlayer sandwiched between the high-melting-point base materials, in which the interlayer strength is typically lower than that of the base material. When this butt-joined composite is loaded uniaxially in the direction perpendicular to the plane of the brazing layer, the tensile strength is found to be much higher than that of the braze. This seems to violate the iso-stress condition in such a butt-joint serial configuration. The stress triaxiality has been usually ascribed, but without a quantitative rationalization, as being responsible for this tensile strength enhancement. Here a complete finite element simulation has been conducted to study the dependence of triaxiality and strength enhancement on geometric and material parameters. Two asymptotic limit solutions (based on Bridgman and Xia–Shih solutions, respectively) have been identified to understand the simulation results. The critical role of void evolution has been revealed when making a quantitative comparison to available experiments. In addition, ductility of the brazed joint, which has not been fully addressed in literature, is investigated by the Gurson–Tvergaard–Needleman model.

https://doi.org/10.1007/s11661-020-05984-x

I. INTRODUCTION

IN contrast to fusion welding in which base and filler materials are all melted, the brazing technique melts a soft and low-melting-point material, such as silver-based filler, and fills into the narrow gap between two base materials, such as stainless steels.[1–3] The operation temperature is much lower than the melting point of the base materials, and thus their microstructural features remain unchanged. The convenience of this technique and the soundness and fidelity of the end products ensure a wide spectrum of applications and extensive industrial and academic studies, such as their usage in automotive, aerospace, and electronic industries,[4–9] their processing–microstructure–property relationship,[10–12] and more importantly their structural integrity.[13–18] The last one becomes crucial as the brazing technique becomes a critical repair tool for turbine alloys at high-temperature operation conditions.

There are two practical issues that have not been fully understood. First, the low yield strength of the brazing layer may jeopardize the structural integrity of this composite structure. Nevertheless, when loaded in the direction perpendicular to the plane of the brazing layer, it has been found that the brazed joint has a much higher tensile strength than that of the soft interlayer. Refer to the experimental data[3] in Figure 1 and the geometric setup in Figure 2. The ultimate tensile strength (UTS) of a pure cast silver is about 100 MPa, but the UTS of silver brazed joint between two steel bars can be as high as 800 MPa when the thickness-to-diameter ratio, t/D, is less than one thousandth. This seems to violate the iso-stress condition since the "weakest" link dictates the overall behavior in a composite structure in which its components are connected in series. Second, the role of initial defect (voids, or incomplete filling) on the composite strength and also

XIN CAI is with the School of Petroleum Engineering, China University of Petroleum, Qingdao 266580, China and also with the Department of Materials Science and Engineering, University of Tennessee, Knoxville, TN 37996. YANFEI GAO and XUE WANG are with the Department of Materials Science and Engineering, University of Tennessee. Contact e-mail: ygao7@utk.edu WEI ZHANG and ZHILI FENG are with the Materials Science and Technology Division, Oak Ridge National Laboratory, Oak Ridge, TN 37831. Contact e-mail: fengz@ornl.gov WEI LIU and XINPU SHEN are with the School of Petroleum Engineering, China University of Petroleum. Contact e-mail: liu.wei@upc.edu.cn WEI ZHANG is with the Department of Materials Science and Engineering, Ohio State University, Columbus, OH 43210. ZHENZHEN YU is with the Department of Metallurgical and Materials Engineering, Colorado School of Mines, Golden, CO 80401. Contact e-mail: zyu@mines.edu

Manuscript submitted March 12, 2020.
Article published online September 5, 2020

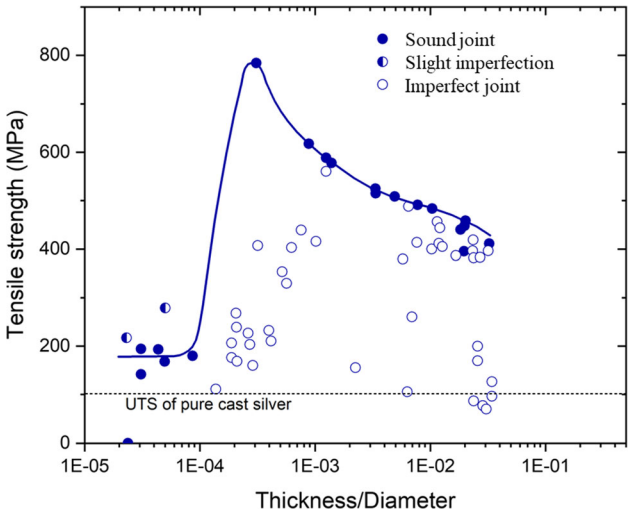

Fig. 1—The uniaxial tensile strength of a butt joint with a soft brazing interlayer (cast silver) sandwiched between base materials (4340 steel). Data are compiled from the ASM Handbook.[3]

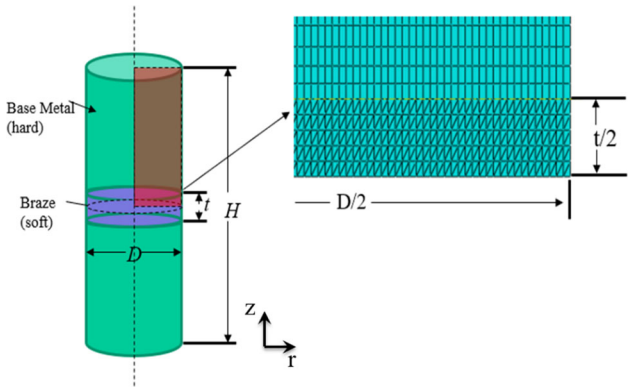

Fig. 2—Schematic illustration of the axisymmetric finite element simulation, geometric parameters, and representative meshes.

the failure behavior has not been fully understood. Since the interlayer is extremely thin, it is difficult to realize a defect-free wetting of the brazing layer into the gap between base materials. In such circumstances, the tensile strength of the composite can dramatically drop but is still higher than the UTS of the silver layer, as shown in the left portion of Figure 1. Similar observations have been reported recently for Ni-base superalloy brazed joints.[7]

Since the strength enhancement is only found when $t/D << 1$, it is necessary to consider the three-dimensional nature of the deformation field in the interlayer. This phenomenon is often attributed to the triaxial constrain effect which results into a lower Mises stress in the brazed interlayer than that far away in the base material. Nevertheless, several drawbacks are noted that prevent a quantitative predictive understanding. First, can we develop approximate solutions for the dependence of stress triaxiality, including its magnitude and in-plane distribution, on geometric and material parameters? Most importantly, is there an upper bound of the stress triaxiality? Second, how is the superposition of a triaxial stress state onto a uniaxial one able to increase the yield strength? Since metal plasticity does not depend on the hydrostatic stress, the underlying reason must lie on a stress analysis. Third, ductility of brazed joints has received little attention in literature, and especially a quantitative prediction of the role of initial voids (which is f_0 in Figures 11, 12, 13, 14, and 15) on the strength and ductility of the composite remains elusive. Quantitative answers to the above questions will certainly improve our understanding of this phenomenon and also help develop new structural and material design rules.

This paper is arranged as follows. An axisymmetric finite element model is constructed in Section II, from which the overall tensile strength will be calculated with respect to a wide range of geometric and material parameters. In addition to the standard Mises plasticity, the Gurson–Tvergaard–Needleman (GTN) model[19–23] is employed to predict the role of damage evolution in strength degradation and ductility limit of this composite structure. Section III reports the numerical results, with a focus on the dependence of triaxial and deviatoric stress states on t/D and the strength ratio of interlayer and base materials. These observations have motivated us to develop two asymptotic solutions, one based on the Bridgman solution of notched bars[24–27] and the other based on Xia–Shih prediction of the fracture energy using the void model.[28,29] As will be shown in Section IV, a quantitative comparison to available experiments requires strength and ductility simulations by the GTN model. Concluding remarks and suggestions for future work will be presented in Section V.

II. PROBLEM FORMULATION

In the axisymmetric finite element setup in Figure 2, a cylindrical rod with the brazed interlayer in the center is subjected to a faraway tensile load. The entire sample size, H, is much larger than the rod diameter, D, so that the only geometric parameter is t/D. In order to avoid using meshes with extremely high or low aspect ratios, calculations with $t/D < 0.01$ require very fine meshes, leading to a typical number of about 10,000 elements. The mesh size e in the brazed joint is small enough to attain numerical convergence and satisfactory accuracy. For our thinnest case, our simulations ensure a mesh size of $e/t = 0.1$.

For the numerical results presented in Section III, Mises plasticity is used for both base and interlayer materials, with the power-law hardening,

$$\varepsilon = \begin{cases} \frac{\sigma}{E}, & \sigma < \sigma_Y \\ \frac{\sigma_Y}{E}\left(\frac{\sigma}{\sigma_Y}\right)^{1/N}, & \sigma \geq \sigma_Y \end{cases} \quad [1]$$

where E is the Young's modulus, σ_Y is the yield stress, and N is the strain hardening exponent.

A straightforward dimensionless analysis gives the yield strength of the entire composite structure, σ_Y^{total}, as normalized y that of the base material, σ_Y^{base}, by

$$\frac{\sigma_Y^{\text{total}}}{\sigma_Y^{\text{base}}} = \Pi\left\{\frac{t}{D}, \frac{\sigma_Y^{\text{braze}}}{\sigma_Y^{\text{base}}}, \frac{\sigma_Y^{\text{base}}}{E_{\text{base}}}, \frac{E_{\text{braze}}}{E_{\text{base}}}, \nu_{\text{base}}, \nu_{\text{braze}}, N_{\text{base}}, N_{\text{braze}}\right\}, \quad [2]$$

where ν is Poisson's ratio. Representative stress–strain curves as shown later in Figure 13 clearly indicate the yield strength. The three dimensionless parameters for elastic properties, *i.e.*, $E_{\text{braze}}/E_{\text{base}}$, ν_{base}, and ν_{braze}, can be further reduced to two Dundurs parameters,[30] which are, however, unnecessary since t/D and $\sigma_Y^{\text{braze}}/\sigma_Y^{\text{base}}$ are the most important parameters. In our parametric studies, we simply set $\nu_{\text{base}} = \nu_{\text{braze}} = 0.3$, $E_{\text{braze}}/E_{\text{base}} = 1$, $\sigma_Y^{\text{base}}/E_{\text{base}} = 1/1000$, $N_{\text{base}} = 0$, and $N_{\text{braze}} = 0$ or 0.2. Later in this paper, when compared to available experiments, actual material parameters are used as given in Tables I and II. Representative values in these tables also suggest a possible strength variation over a factor of 10.

For the numerical results presented in Section IV, the GTN model is used that specifies the yield potential by Reference 19

$$\Phi = \left(\frac{\sigma_e}{\bar{\sigma}}\right)^2 + 2q_1 f^* \cosh\left(\frac{3q_2\sigma_m}{2\bar{\sigma}}\right) - \left(1 + (q_1 f^*)^2\right) = 0, \quad [3]$$

where σ_e denotes the effective stress, σ_m the mean stress, $\bar{\sigma}$ an equivalent tensile flow stress representing the actual microscopic stress state in the matrix (*i.e.*, Eq. [1]), and q_1 and q_2 are dimensionless constants (taken as 1.5 and 1.0, respectively, in our simulations). The modified void volume fraction, f^*, relates to the void volume fraction f through

$$f^* = \begin{cases} f, & f < f_C \\ f_C + \frac{(1q_1 - f_C)(f - f_C)}{f_E - f_C}, & f \geq f_C \end{cases} \quad [4]$$

where f_C is the critical value for void coalescence to take place and f_E is for the final failure at which there is a complete loss of stress carrying capacity in the material (taken as 0.1 and 0.3, respectively, in our simulations according to Tvergaard[19]). Only void growth is considered here, as given by

$$\dot{f} = (1 - f)\dot{\varepsilon}_{kk}^p, \quad [5]$$

where $\dot{\varepsilon}_{kk}^p$ is the trace of the plastic strain rate tensor $\dot{\varepsilon}_{ij}^p$. Summation convention is implied for repeated Latin indices. Consequently, the only dimensionless parameter, to be added to Eq. [2], is the initial void volume fraction, f_0.

Table I. Material Properties Used in the Comparison to Experiments in Fig. 1 from the ASM Handbook.[3]

Material	E(GPa)	V	σ_Y(MPa)	UTS(MPa)
4340 Steel	200	0.3	690	950
Silver	100	0.3	100	—

III. STRENGTH ENHANCEMENT

In this section, finite element simulation results using Mises plasticity are presented first, followed by the yield-surface analysis. We then derive two asymptotic behaviors, one being the analytical solutions based on the Bridgman notch analysis[24–27] and the other being the Xia–Shih fracture energy prediction.[28,29]

A. *Numerical Results and Yield-Surface Analysis*

Because $N_{\text{base}} = 0$ and the interlayer is softer than the base, the yield stress and the onset of interlayer necking happen together on the overall engineering stress–strain curves. Contour plots of $\sigma_Y^{\text{total}}/\sigma_Y^{\text{braze}}$ and $\sigma_Y^{\text{total}}/\sigma_Y^{\text{base}}$ are given in Figures 3(a) and (b), respectively, for $N_{\text{braze}} = 0$, and in Figures 4(a) and (b), respectively, for $N_{\text{braze}} = 0.2$. When $t/D << 1$ and $\sigma_Y^{\text{braze}}/\sigma_Y^{\text{base}} \to 1$, the composite strength approaches σ_Y^{base}, which clearly is the upper bound limit. While N_{braze} affects the necking condition for a homogeneous braze material, the fact that the braze layer is thin and sandwiched in two hard materials leads to negligible effect in the overall strength and necking condition. Results with $\nu_{\text{braze}} = 0.495$ (not shown for brevity) are also indistinguishable, suggesting that the elastic incompressibility is not relevant in these observations.

A stress state can be described by the triaxiality factor,

$$T = \frac{\sigma_m}{\sigma_e}, \quad [6]$$

where σ_m and σ_e are mean stress and Mises effective stress, respectively. For example, a uniaxial tensile stress state gives this ratio of mean stress to Mises effective stress as 1/3. A question that naturally arises from Figures 3 and 4 is how the stress triaxiality and strength enhancement are related, both qualitatively and quantitatively. This can be illustrated nicely in the principal stress space in Figure 5. Mises plasticity does not depend on the mean stress, so that the yield surface is a cylinder with its axis lying along the mean stress direction (*i.e.*, [111] if using the crystallographic notation). Note that the dashed curves with three representative values of f_0 are modified yield surfaces in the GTN model (*i.e.*, Eq. [3]), which are of capsule shape rather than cylinders. For a homogeneous braze material under uniaxial tension, the stress state corresponds to Point A in Figure 5,

Table II. Material Properties Used in the Comparison to Experiments in Riggs.[7]

Material	E(GPa)	V	σ_Y(MPa)	UTS(MPa)
IN718	200	0.3	1170	1500
CMSX	200	0.3	930	1060
BNi2-ASZ	180	0.3	1400	—
BNi2-ISZ	180	0.3	200	—

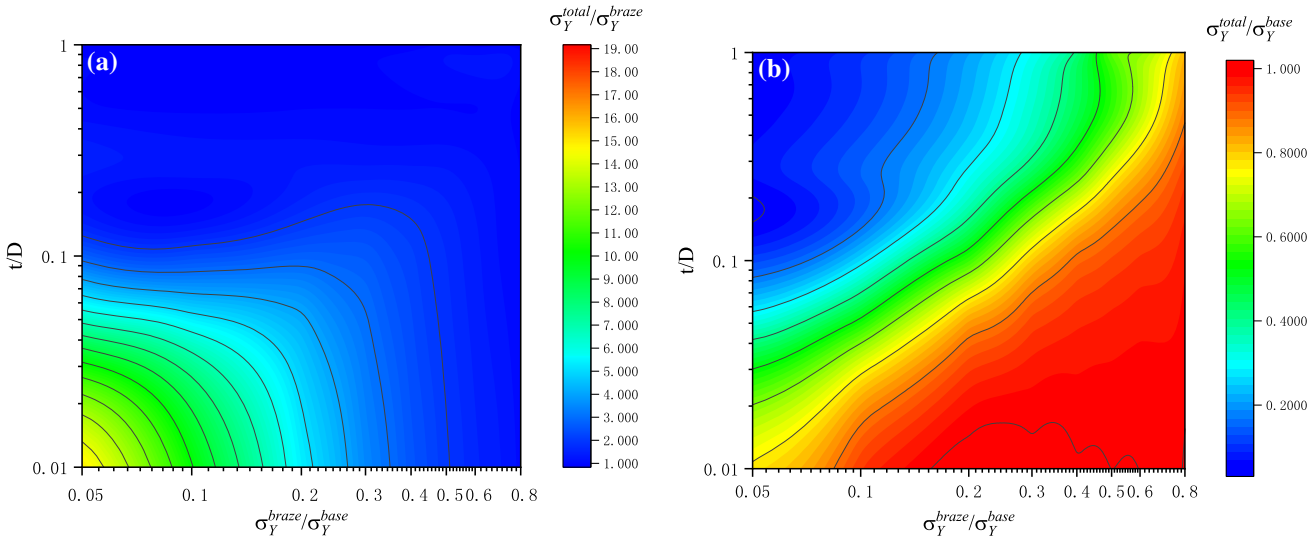

Fig. 3—Contour plots of (*a*) $\sigma_Y^{\text{total}}/\sigma_Y^{\text{braze}}$ and (*b*) $\sigma_Y^{\text{total}}/\sigma_Y^{\text{base}}$ with respect to t/D and $\sigma_Y^{\text{braze}}/\sigma_Y^{\text{base}}$. Both materials are elastic-perfectly plastic (*i.e.*, $N=0$).

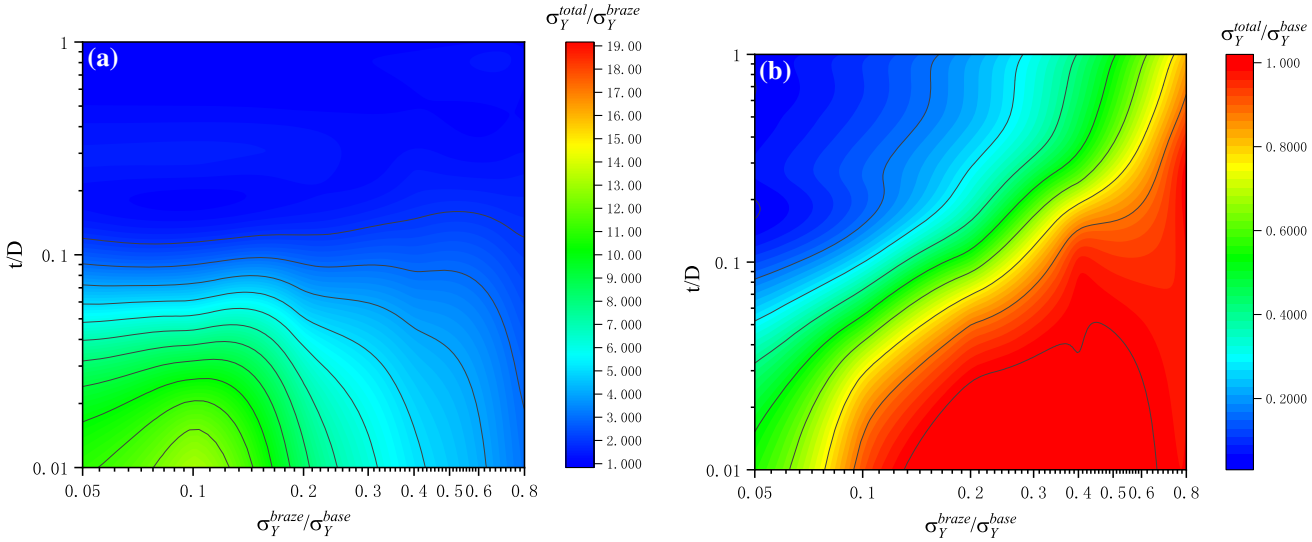

Fig. 4—Contour plots of (*a*) $\sigma_Y^{\text{total}}/\sigma_Y^{\text{braze}}$ and (*b*) $\sigma_Y^{\text{total}}/\sigma_Y^{\text{base}}$ with respect to t/D and $\sigma_Y^{\text{braze}}/\sigma_Y^{\text{base}}$. For the brazing layer, $N = 0.2$. The base material is elastic-perfectly plastic.

$$\boldsymbol{\sigma} = \begin{bmatrix} 0 & 0 & 0 \\ 0 & 0 & 0 \\ 0 & 0 & \sigma_{zz} \end{bmatrix}, \qquad [7]$$

and yield happens at $\sigma_{zz} = \sigma_Y^{\text{braze}}$.

For our composite structure, the stress state in the brazing layer consists of both hydrostatic and deviatoric components, given by Point B in Figure 5,

$$\boldsymbol{\sigma} \approx \begin{bmatrix} 1 & & \\ & 1 & \\ & & 1 \end{bmatrix} \sigma_m + \begin{bmatrix} -\frac{1}{3} & & \\ & -\frac{1}{3} & \\ & & \frac{2}{3} \end{bmatrix} \sigma_e, \qquad [8]$$

which is obviously approximate since the stress state is not uniform as will be shown in Figures 6 and 8. The overall tensile strength corresponds to the stress component σ_{zz} when yield happens,

$$\sigma_Y^{\text{total}} \approx \sigma_m + \frac{2}{3}\sigma_Y^{\text{braze}} = \left(T + \frac{2}{3}\right)\sigma_Y^{\text{braze}}. \qquad [9]$$

The above dependence of σ_Y^{total} on T can also be visualized by the angle ϕ in Figure 5, which relates to the stress triaxiality by

$$\tan\phi = \frac{\sqrt{3}\sigma_m}{\sqrt{2/3}\sigma_Y} = \frac{3}{\sqrt{2}}T. \qquad [10]$$

At Point A, $T_A = 1/3$. As the stress state moves from Point A to Point B and further, $T \to \infty$ and $\phi \to \pi/2$.

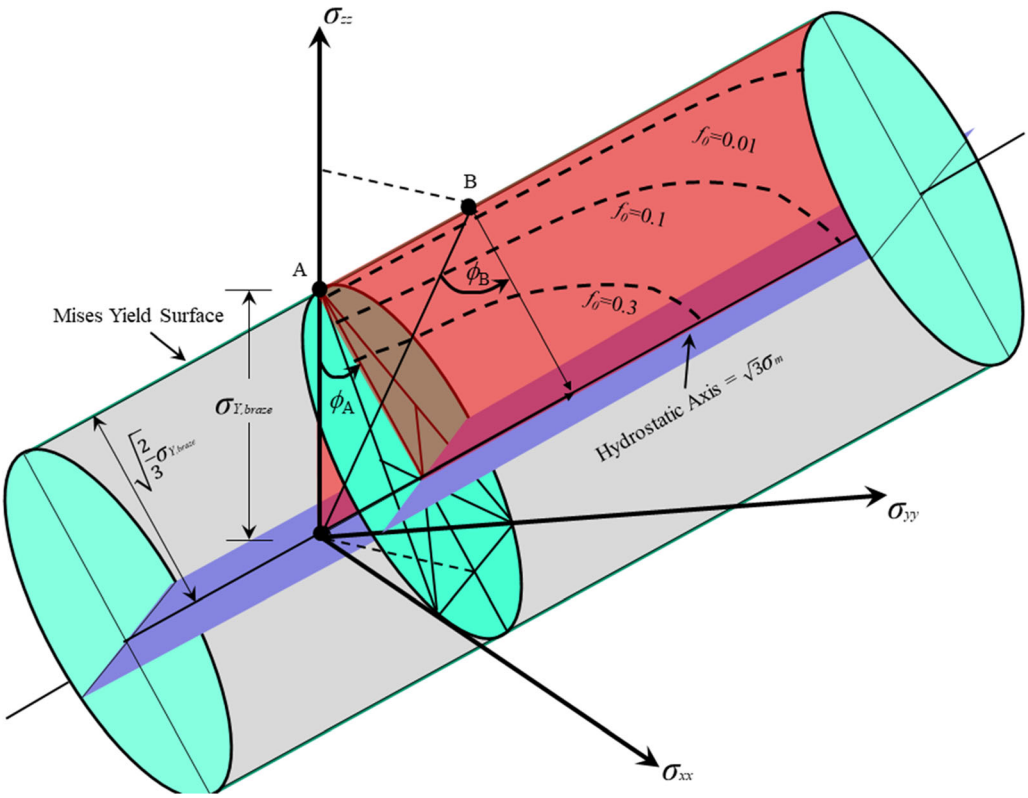

Fig. 5—The yield surface in Mises plasticity is a cylinder in the principal stress state. A uniaxial loading of a homogeneous material will take the path of OA ($T = 1/3$), while the butt joint structure corresponds to the stress state at B ($T > 1/3$) that has a superposition of hydrostatic and deviatoric stresses as given in Eq. [8]. Stress triaxiality T is proportional to $\tan\phi$. Dashed curves are modified yield loci with several representative values of initial porosity, f_0, in Eq. [3].

B. *Bridgman Asymptote*

With a fixed ratio of $\sigma_Y^{\text{braze}}/\sigma_Y^{\text{base}} = 0.05$, Figure 6 shows the stress triaxiality distributions along the central cross-sectional plane ($z = 0$) and the plane of (r, z), with respect to a wide range of the geometric ratio of t/D. With the decrease of t/D, T not only increases but also distributes more evenly along the r direction, at which the approximate solution in Eq. [9] becomes more accurate. In order to find out an approximate solution for the stress triaxiality, we notice the severe necking at a low t/D, which resembles the Bridgman problem for the notched bar in Figure 7 when the diameter of the notched zone is not much smaller than that of the base material.

The Bridgman solution is given by Reference 24

$$T = \frac{\sigma_m}{\sigma_e} \approx \frac{1}{3} + \ln\left(\frac{a}{2\rho} + 1\right), \qquad [11]$$

where a is the outside radius of the cross section and ρ is the radius of curvature at the notch root. Without the notch, the stress field is uniaxial and thus $T = 1/3$. It should be noted that the Bridgman solution works for the fully plastic deformation, but not for the elastic deformation. In our simulations in Figure 6, we notice the severe necking because of the soft brazing layer, so that we can take $a \approx D/2$ and $\rho \approx t/2$. Of course, our problem differs from Bridgman setup in Figure 7, for we have a soft interlayer. Nevertheless, the condition of $t/D << 1$ suggests that the fully plastic field can still borrow the Bridgman solution, as our goal is to develop an approximate yet analytical solution for Eq. [9]. Consequently, combining Eqs. [9] and [11] gives our Bridgman asymptotic solution,

$$\frac{\sigma_Y^{total}}{\sigma_Y^{braze}} \approx 1 + \ln\left(\frac{D}{2t} + 1\right). \qquad [12]$$

This predicted logarithmic dependence on t/D agrees well with the trends in Figures 3, 4, and 6. It should also be pointed out that the above result resembles the solution of compression tests with an infinite friction between specimen and loading platens.

C. *Xia–Shih Asymptote*

With a fixed ratio of $t/D = 0.01$, Figure 8 shows the stress triaxiality distributions with respect to a wide range of the strength ratio of $\sigma_Y^{\text{braze}}/\sigma_Y^{\text{base}}$. For such a thin brazing interlayer, the softer the brazing material, the stress triaxiality indeed goes higher, but the distribution becomes less uniform. As indicated by the example with $\sigma_Y^{\text{braze}}/\sigma_Y^{\text{base}} = 0.1$, the highest value of T is located in a ring of about $D/6$ away from the outer surface. This dependence of T distribution on

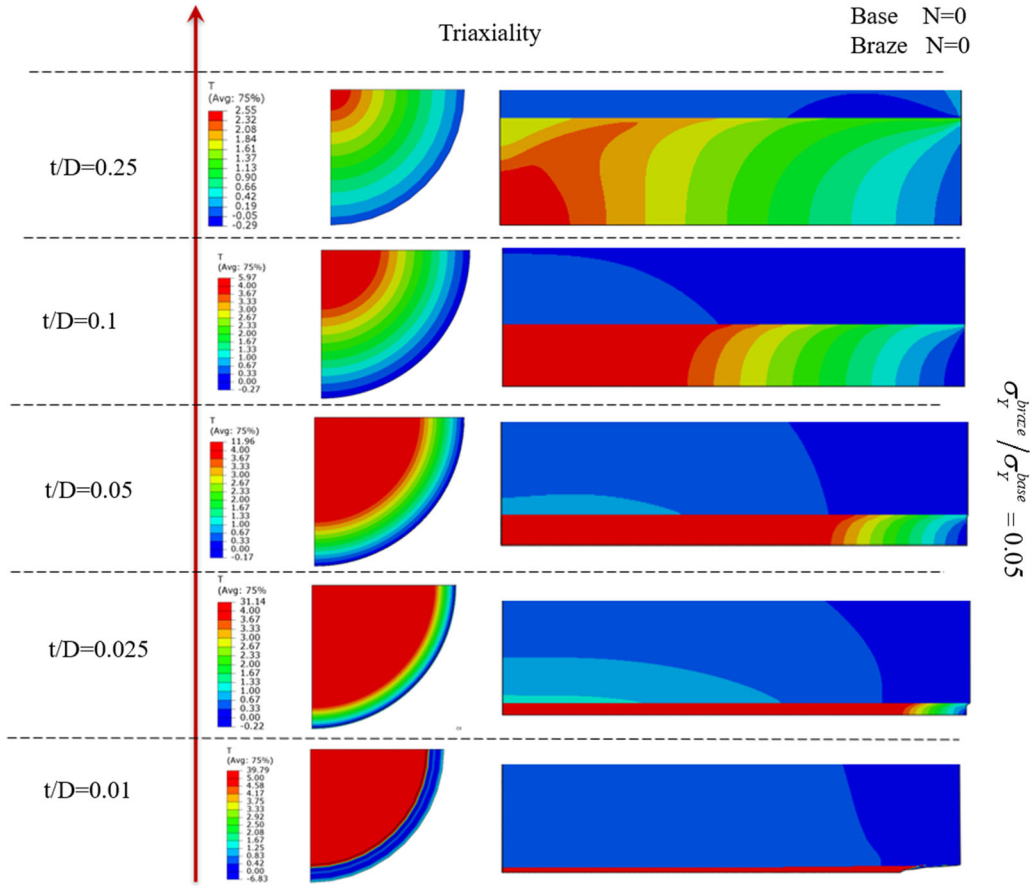

Fig. 6—Contour plot of the triaxiality distribution in the cross section ($z = 0$) and (r, z) plane with respect to several values of t/D.

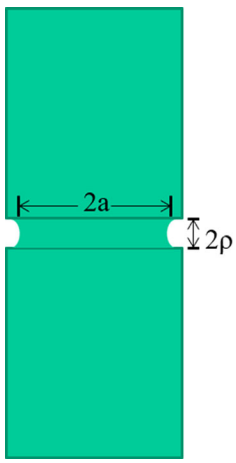

Fig. 7—Construction of the Bridgman limit solution from a notched bar.

$\sigma_Y^{\text{braze}}/\sigma_Y^{\text{base}}$ is rationalized in this subsection by the Xia–Shih model.[28]

As the soft brazing interlayer can be viewed as softened by initial voids or porosities, our problem resembles the fracture energy predictions by Xia and Shih,[28] using a cell model ahead of the crack tip in Figure 9. In the cells far away from the crack tip, the porosity is the initial value, f_0. Voids can be either explicitly simulated or smeared out by the GTN model. The crack tip is determined when the porosity reaches f_E at which the porosity coalesces to form new crack surfaces and therefore the crack advances. Consequently, this setup leads them to compute the entire R-curve as shown in Figure 10. The initial fracture energy scales as $\Gamma_0 \propto \sigma_Y d$, and the fracture energy eventually reaches a steady-state plateau value, Γ_{ss}. The critical extension of the crack, $\Delta a_{crt}/d$, to reach this steady-state value is sensitive mostly to f_0 and N.

It should be reminded again that our goal in this subsection is to provide a mechanistic interpretation of the triaxiality distribution in Figure 8, especially the "annular" one for the soft interlayer. Because of the presence of the soft brazing layer, the overall deformation leads to the appearance of notch that resembles a ductile crack tip for a very small t/D ratio in Figure 8. Next, we make the analogy between a very soft interlayer (bottom row in Figure 8) to a highly damaged strip (high f_0 value in Figure 9). With a small initial porosity (*i.e.*, corresponding to a not-so-soft interlayer in our problem) and a large strain hardening exponent, such as $f_0 = 0.001$ and $N = 0.2$, $\Delta a_{crt}/d$ is about 20. In other words, the crack-tip plastic zone is considerably large. Referring to our geometric setup in Figure 8 that resembles an externally circular crack, the large crack-tip plastic zone extends from outside towards the center of the circular brazing plane, thus leading to the

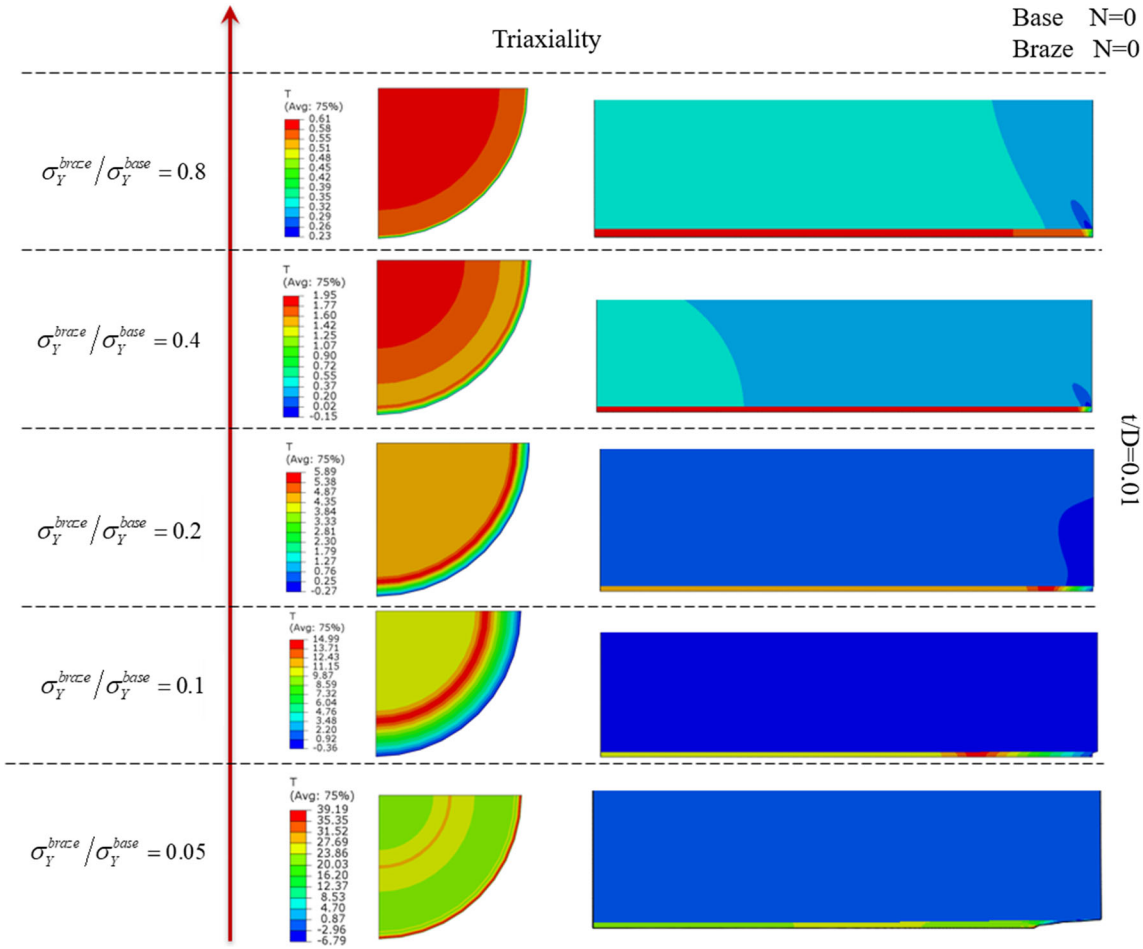

Fig. 8—Contour plot of the triaxiality distribution in the cross section ($z = 0$) and (r, z) plane with respect to several values of $\sigma_Y^{\text{braze}}/\sigma_Y^{\text{base}}$.

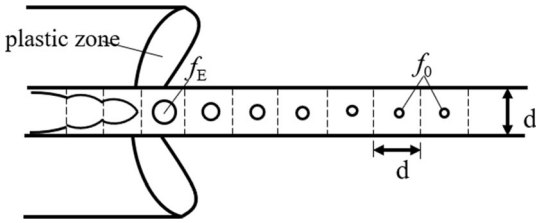

Fig. 9—A ductile crack growth model, as schematically illustrated by following the work of Xia and Shih.[28]

accumulation of T as shown by the actual simulation results in the top rows in Figure 8 and schematically in the top right in Figure 10. On the contrary, with a large initial porosity (*i.e.*, corresponding to a soft interlayer in our problem), $\Delta a_{crt}/d$ is small. For the setup in Figure 8, this corresponds to a small crack-tip process zone, so that the peak value of T lies not far from the boundary of $r = D/2$, as shown by the simulation results in the bottom rows in Figure 8 and schematically in the lower right in Figure 10. Consequently, using the numerical results from Xia and Shih,[28] the predicted dependence of $\sigma_Y^{\text{total}}/\sigma_Y^{\text{base}}$ on $\sigma_Y^{\text{braze}}/\sigma_Y^{\text{base}}$ in our problem agrees nicely with the trends in Figure 8.

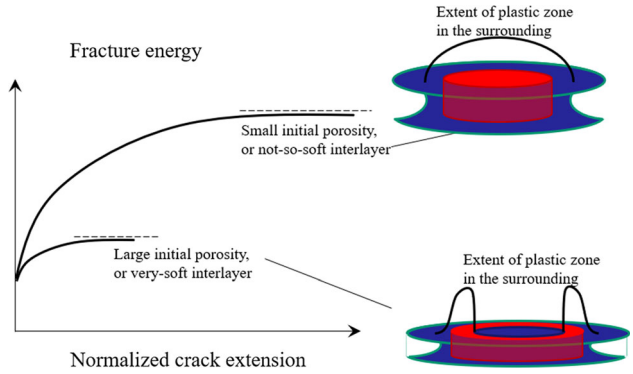

Fig. 10—Schematic illustration of the fracture energy with respect to the normalized crack extension, $\Delta a/d$. The steady-state limit, Γ_{ss}, increases with the decrease of initial porosity and the increase of interlayer strength.

Finally, we should point out that the use of Xia–Shih model is to provide a mechanistic interpretation of the annular distribution of stress triaxiality in Figure 8 where finite element simulations are not performed with the GTN model.

IV. DAMAGE ANALYSIS AND EXPERIMENTAL COMPARISONS

A. *Ductility Degradation*

In brazed joints, defects are inherently found within the interlayer due to incomplete gap filling, especially when the interlayer is very thin. Experimental results in Figure 1 demonstrate the sensitivity to such an initial defect. Before making any attempts to compare to available experiments, we need to first conduct a damage analysis. Starting from results in Figure 4 and using $f_0 = 0.02$ in our GTN model, Figure 11 shows that the composite strength decreases dramatically from the no-damage results, with respect to the decrease of t/D and $\sigma_Y^{\text{braze}}/\sigma_Y^{\text{base}}$. Representative failure modes, as shown by the contours of f in Figure 12, demonstrate the normal crack at the center and shear crack near the perimeter.

For the two cases in Figure 12, their corresponding engineering stress–strain curves are given in Figure 13(a), showing that thicker interlayer case (Figure 12(b)) leads to a higher ductility than the thinner interlayer case (Figure 12(a)). Interestingly, this finding is opposite to the no-damage simulation results, as also plotted in Figure 13(a), which shows the thinner interlayer case has a longer failure strain. As results in Figure 13(a) correspond to the cases in Figure 6, additional simulations were conducted to compare to the cases in Figure 8 where t/D is fixed. The ductility of no-damage cases extends to very far away and goes beyond the simulation accuracy. Nevertheless, the damage model is trustworthy and predicts that the soft interlayer case has a reduced ductility. Results in Figure 13 can be understood and summarized from the underlying mechanisms that dictate the ductility, as presented below.

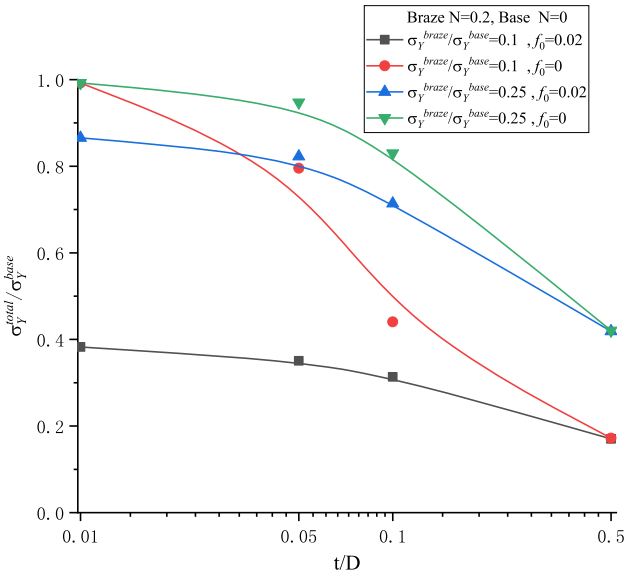

Fig. 11—The composite strength degrades with the consideration of damage evolution.

- For interlayers without damage (*i.e.*, not employing the GTN model) or with high quality (*i.e.*, extremely low f_0 when using the GTN model), the ductility is determined by necking. Because the necking strain of the interlayer material is typically much lower than that of the base material, the ductility will be retained as that of the base material when the interlayer is thin. Thicker interlayers will reduce both the overall strength and ductility.
- For "poor" interlayers (*i.e.*, noticeable f_0 in the GTN model), the ductility is dictated by the void process in the interlayer. Under such circumstances, while the Bridgman asymptote predicts a higher composite strength for a thinner interlayer, the corresponding ductility unfortunately gets poorer. On the other hand, as the Xia–Shih asymptote predicts a higher composite strength for a harder interlayer, the corresponding ductility gets better accordingly.

B. *Comparisons to Literature Experiments*

Two sets of literature experimental data are examined from our damage simulations, including the data in ASM handbook[3] (Figure 14) and those in a doctoral thesis from The Ohio State University (OSU)[7] (Figure 15). In Figure 14, the base and braze materials are 4340 steel and cast silver, respectively, with their mechanical properties given in Table I. The measured UTS of the composite lies between our simulation results with $f_0 = 0$ and 0.02. For a higher t/D, experimental data are closer to simulations with $f_0 = 0.02$, which can be interpreted by the tendency of having more solidification-induced porosities in the thick interlayer. In Figure 15, two types of Ni-base superalloys, IN718 and CMSX-4, are used as base materials, and the brazing interlayer is BNi2, with their mechanical properties given in Table II. Since the filler material experiences melting and solidification, Riggs[7] has identified two regimes of the brazing layer: the hard centerline eutectic zone or athermally solidified zone (ASZ), and the soft isothermally solidified zone (ISZ). Our simulations using the GTN model do not show much reduction of the composite strength when changing f_0 from 0 to 0.02, most likely because of the high strength of BNi2 ASZ intermediate layer. Additional calibration of model parameters is required to make improved comparisons to these experiments.

V. CONCLUSIONS

Brazing technique has found widespread applications and successes in automotive, aerospace, and electronic industries. However, two critical issues have not been fully understood, including (1) the enhanced composite strength than that of the brazing interlayer, and (2) the role played by the void and damage processes on strength and ductility of the composite structure.

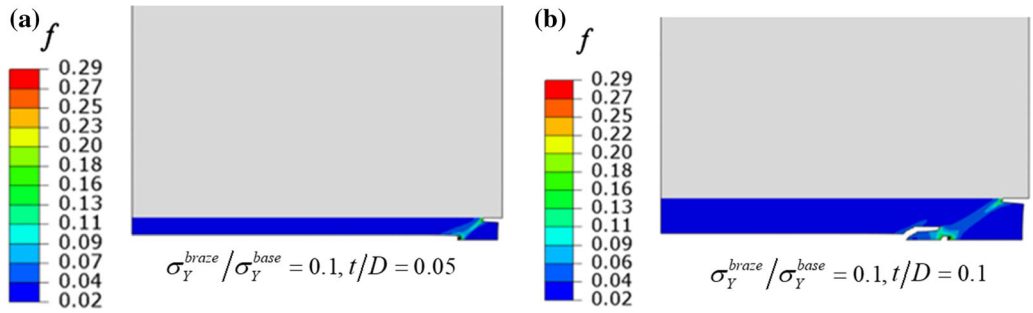

Fig. 12—Contour plot of the porosity, f, in the brazing interlayer with $\sigma_Y^{\text{braze}}/\sigma_Y^{\text{base}} = 0.1$, $t/D = 0.05$ in (a) and 0.1 in (b). Elements with porosity reaching f_E have been deleted, showing the central normal crack and the shear crack near the perimeter.

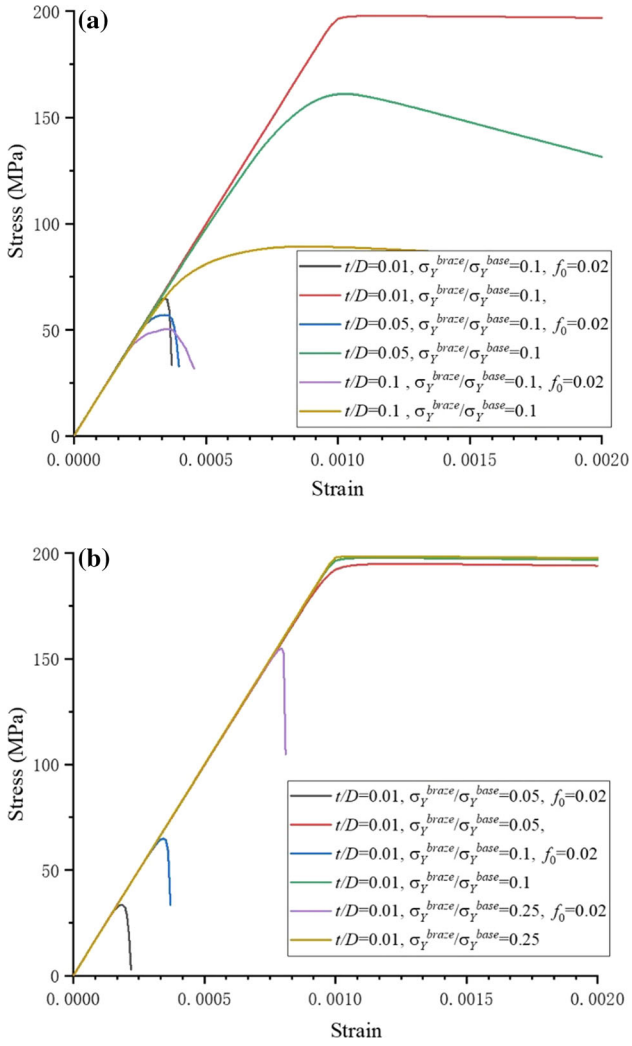

Fig. 13—Representative stress–strain curves: (a) $\sigma_Y^{\text{braze}}/\sigma_Y^{\text{base}} = 0.1$, varying t/D, and with or without initial porosity (refer to Fig. 6 for contour plots of no-damage cases); (b) $t/D = 0.01$, varying $\sigma_Y^{\text{braze}}/\sigma_Y^{\text{base}}$, and with or without initial porosity (refer to Fig. 8 for contour plots of no-damage cases).

For the first issue, based on extensive finite element simulations of the stress–strain curves, together with the calculated stress triaxiality distribution, the observed strength enhancement can now be quantitatively understood. The superposition of a triaxial stress state will

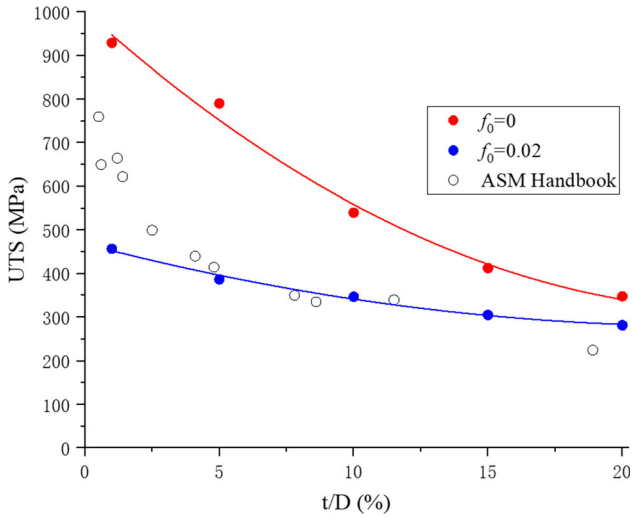

Fig. 14—Comparison between simulated (solid curves and filled symbols) and experimental (open symbols) strength data. Experimental data are compiled from the ASM Handbook.[3]

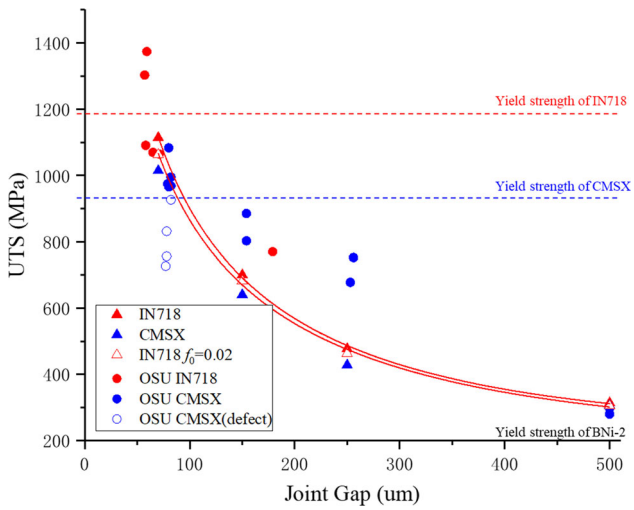

Fig. 15—Comparison between simulated (solid curves and triangles) and experimental (circles) strength data. Experimental data are compiled from a doctoral thesis in The Ohio State University.[7] See text for details on the schematic illustration of the multilayered structure in the braze.

increase the tensile yield strength by $(T-13)\sigma_Y^{\text{braze}}$, according to Eq. [9]. A geometric illustration is presented in Figure 5 by the yield surface in the principal stress space. Two asymptotic solutions are derived to explain the limit behavior of finite element simulation results in Figures 3 and 4. The Bridgman asymptote in Eq. [12] explains the dependence on t/D, while the Xia–Shih asymptote in Figure 10 rationalizes the dependence on $\sigma_Y^{\text{braze}}/\sigma_Y^{\text{base}}$.

For the second issue, damage evolution has been computed in the three-dimensional manner. Along the Bridgman asymptote, the strength improvement is accompanied with the ductility degradation. However, along the Xia–Shih asymptote, the improvement of strength and ductility occurs simultaneously. Experimental comparisons can only be made quantitative by considering the damage evolution, as shown by our numerical simulations based on the GTN model. Particularly, the initial porosity and microstructural features in the brazing interlayer need to be carefully quantified. These damage simulation results suggest useful directions for design reliable brazed joints, because the actual experiments may not retain a complete filling (*e.g.*, Figure 1) and the widespread onset of damage near the edge may suggest microstructural or other approaches to inhibit its occurrence.

ACKNOWLEDGMENTS

This work has been supported by the China Scholarship Council (XC), the US National Science Foundation DMR-1809640 (YFG) and CMMI-1847630 (ZZY), the Center for Materials Processing at University of Tennessee (XW), and the US Department of Energy, Office of Vehicle Technology, under a prime contract with Oak Ridge National Laboratory (WZ and ZLF).**DATA AVAILABILITY**

Data contained in this paper are available upon request to the corresponding authors.

REFERENCES

1. R.S. Rosen and M.E. Kassner: *ASM Handbook*, ASM International, Cleveland, 1993.
2. American Welding Society (AWS): *Brazing Handbook*, American Welding Society, Miami, 2007.
3. T. Lienert, T. Siewert, S. Babu, and V. Acoff: *ASM Handbook*, ASM International, 2011, vol. 6A Welding Fundamentals and Processes.
4. J.W. Lee, J.H. McMurray, and J.A. Miller: *Weld J.*, 1985, vol. 64, pp. 18–21.
5. T. Zaharinie, R. Moshwan, F. Yusof, M. Hamdi, and T. Ariga: *Mater. Des.*, 2014, vol. 54, pp. 375–81.
6. R.K. Shiue, S.K. Wu, and S.H. Yang: *Metall. Mater. Trans. A*, 2017, vol. 48A, pp. 735–44.
7. B.E. Riggs: *Multi-scale computational modeling of Ni-base superalloy brazed joints for gas turbine applications*. PhD Thesis, The Ohio State University, 2017.
8. M. Gao, B. Schneiderman, S.M. Gilbert, and Z. Yu: *Metall. Mater. Trans. A*, 2019, vol. 50A, pp. 5117–27.
9. M. Way, J. Willingham, and R. Goodall: *Int. Mater. Rev.*, 2020, vol. 65, pp. 257–85.
10. S.K. Tung, L.C. Lim, and M.O. Lai: *Scripta Mater.*, 1995, vol. 33, pp. 1253–59.
11. A. Elrefaey and W. Tillmann: *J. Alloys Compd.*, 2009, vol. 487, pp. 639–45.
12. J. Ruiz-Vargas, N. Siredey-Schwaller, N. Gey, P. Bocher, and A. Hazotte: *J. Mater. Process. Tech.*, 2013, vol. 213, pp. 20–29.
13. A.J. West, H.J. Saxton, A.S. Tetelman, and C.R. Barrett: *Metall. Trans.*, 1971, vol. 2, pp. 1009–17.
14. Y.H. Yu and M.O. Lai: *J. Mater. Sci.*, 1995, vol. 30, pp. 2101–07.
15. J. Mackerle: *Model. Simul. Mater. Sci. Eng.*, 1997, vol. 5, pp. 159–85.
16. Y.W. Lee, J.H. Kim, Y.S. Song, and C.S. Seok: *Solid State Pheno.*, 2007, vols. 124–126, pp. 1673–76.
17. M.K. Ghovanlou, H. Jahed, and A. Khajepour: *Eng. Fract. Mech.*, 2014, vol. 120, pp. 43–59.
18. W. Jiang, W. Woo, and S.T. Tu: *Mater. Des.*, 2015, vol. 72, pp. 63–71.
19. V. Tvergaard: *Adv. Appl. Mech.*, 1990, vol. 27, pp. 83–151.
20. Z. Xue, M.G. Pontin, F.W. Zok, and J.W. Hutchinson: *Eng. Frac. Mech.*, 2010, vol. 77, pp. 492–509.
21. K.L. Nielsen and V. Tvergaard: *Eng. Fract. Mech.*, 2010, vol. 77, pp. 1031–47.
22. A.A. Benzerga, J.-P. Leblond, A. Needleman, and V. Tvergaard: *Int. J. Fract.*, 2016, vol. 201, pp. 29–80.
23. Y.F. Gao, Z. Xue, and Z. Yu: *Ext. Mech. Lett.*, 2020, vol. 37, p. 100728.
24. K.M. Flores and R.H. Dauskardt: *Acta Mater.*, 2001, vol. 49, pp. 2527–37.
25. W.D. Li, H. Bei, and Y.F. Gao: *Intermetallics*, 2016, vol. 79, pp. 12–19.
26. W.D. Li, Y.F. Gao, and H. Bei: *Sci. Rep.*, 2016, vol. 6, p. 34878.
27. Y.C. Zhao and Y.F. Gao: *JOM*, 2020, vol. 72, pp. 877–82.
28. L. Xia and C.F. Shih: *J. Mech. Phys. Solids*, 1995, vol. 43, pp. 233–59.
29. Y. Cui, Y.F. Gao, and H.B. Chew: *Int. J. Solids Struct.*, 2020, vols. 200–201, pp. 188–97.
30. Y.F. Gao, H.T. Xu, W.C. Oliver, and G.M. Pharr: *J. Mech. Phys. Solids*, 2008, vol. 56, pp. 402–16.